Quantifying defects in carbon nanotubes undergoing prolonged electrochemical cycling with Raman phase map

Sirshendu Dinda [a,*], Tobias Braun [a], Frank D. Pammer [a], Jaehoon Choi [a], Simon Fleischmann [a], Maximilian Fichtner [a,b]

[a] Helmholtz Institute Ulm (HIU), Helmholtzstr. 11, 89081, Ulm, Germany
[b] Institute of Nanotechnology, Karlsruhe Institute of Technology (KIT), P.O. Box 3640, 76021, Karlsruhe, Germany

ARTICLE INFO

Keywords:
Raman phase map
Raman spectroscopy
Graphitic structure
Defects
Electrocatalytic cycling

ABSTRACT

Electrically conducting graphitic carbon materials are ubiquitous constituents of electrocatalysts and electrochemical energy storage materials. During electrolysis and electrochemical charge-discharge cycles, the carbon matrix is subjected to chemical stress due to drastic changes in the redox environment, the formation of reactive intermediate species and to steric strain caused by intercalation of counter ions. These factors trigger the formation of defects in the graphitic lattice, leading to scattering the charge carriers, thereby reducing the carrier mobility. It is of utmost importance to reliably monitor the graphitic lattice to maintain the integrity of the material and recognize the nature of defects. We have applied statistical Raman measurement technique in conjunction with Raman phase map and Raman ellipse to monitor and quantify the formation of point and line defects in functionalized carbon nanotubes. We also demonstrate how the Raman ellipse in combination with $I_D/I_{D'}$ is a new and powerful analytical tool which can serve to deduce the correct defect generation process in a graphitic lattice exposed to stress during electrochemical cycling. Thus, a deep mechanical insight by "simple" optical spectroscopy can be captured through our proposed Raman phase map analysis.

1. Introduction

Over the past decades, the use of electrochemical energy storage (EES) devices has become widespread in industrial, consumer, and automotive applications. Continuous efforts are being made in research and engineering to enhance the performance of both cathode and anode materials. In this regard, improvement of conductivity and ion diffusion is of particular importance to enable new applications in the area of high energy and high power EES devices [1,2]. Carbon based nano-composites are widely used as active materials, conductive additives, and electrochemical reaction frameworks in electrodes to enhance energy density in EES devices [3,4]. The currently leading EES technology is the Li-ion battery, which relies on a graphite anode as host for intercalating lithium cations. This concept imposes an upper limit on the maximum energy density due to the limited amount of stored lithium ions per mass and volume of the host [5]. Numerous structural modifications and nano-composite design techniques have been employed to modify the anode material to enhance overall performance of the anode as well as to reduce volumetric expansion [6–8].

Low dimensional carbon nanomaterials, such as carbon nanotubes and carbon nano-flakes have been used to fabricate anodes due to their mechanical strengths, high electrical conductivity and tunable surface functionality [8,9]. Furthermore, emerging battery technologies, particularly the sodium ion battery, require the development of new carbon materials, which are tailored for this application [10–12]. Carbon nanomaterials also have been employed to increase coulombic efficiency and enhance charge-transfer kinetics across the electrodes, and thereby improve the tap density [13–15].

In another application field, generation of hydrogen via electrochemical water splitting with surplus renewable energy constitutes an environmentally friendly form of energy storage with even higher energy density. Combining two half-cell reactions, oxygen evolution reaction (OER) where oxidation of water is performed at anode and hydrogen evolution reaction (HER) where H^+ is reduced at cathode, electrolysis of water is carried out [16,17]. In practice this seemingly easy electrochemical process requires a vast amount of energy due to the over-potential required to initiate the cathode and anode reactions. To reduce this problem and facilitate the electrolytic reaction, noble metal

* Corresponding author.
E-mail address: sirshendu.dinda@kit.edu (S. Dinda).

nanoparticles (Pt, Pd) [18], transition metal nanoparticles (Ru, Co, Ni) [19] or transition metal sulfides (CoS) [20] have been used as catalyst. Likewise, carbon materials find wide use in this technology where the sluggish oxygen reduction reaction (ORR) is the main bottleneck. Hence, continuous efforts are made with metal nanoparticle based cathode materials [21]. Lowering the reduction potential of oxygen in ORR process through catalytic activity has also been investigated in combination with several types of heteroatom doped carbon nanotubes, graphene and graphitic flakes such as nitrogen-doped, boron-doped, sulphur-doped [22–25]. In these processes, carbon nanomaterials provide large surface area, good conductivity, tunable morphology, both as matrix for metal nanoparticles and as active materials. To work efficiently, electrode materials for electrolysers need high specific surface area while retaining highly conductivity. Carbon nanotubes (CNTs) and multi-walled carbon nanotubes (MWCNTs) both exhibit these properties and have therefore been tested in a variety of catalysts [26–28].

In the above mentioned technologies, the highly ordered graphitic lattice of sp^2-hybridized carbon atoms provides high conductivity, while disordered, three-dimensional graphitic microstructures provide high specific surface areas [29,30]. In combination, carbon and modified carbon microstructures exhibit superior electrical conductivity, good mechanical integrity, large surface area for electrolyte penetration, and porous structure to accommodate the volume expansion, thus creating a preferred electrode matrix [30].

During electrochemical cycling, the bulk of the carbon material is subjected to substantial structural and chemical stress. The integrity of the sp^2-hybridized carbon lattice is the determining factor for retention the structural shape and electrochemical performance. It is therefore highly desirable to be able to monitor chemical and structural changes to sp^2-backbone in the course of successive electrochemical processes. Continuous electro-cycling will eventually generate different types of defects in the sp^2-honeycomb backbone [31,32]. These include sp^3-defects, vacancy-defects, and boundary-type defects [33].

Raman spectroscopy is a versatile, non-destructive analytical tool for the characterization of carbon nano-phases, in particular for graphitic and nano-graphitic structures (e.g., nanotubes, nanoribbons, ion-bombarded graphene etc.). Monolayer graphene, with a pristine two-dimensional crystalline lattice, has two prominent Raman bands: The G band and the 2D band (also called G′). The G or graphitic band originates from Raman scattering involving one phonon along C–C bonds stretching along hexagonal plane and is located at ~1580 cm ^{1}. The D band appears at ~1340 cm ^{1} in Raman spectrum of the graphitic material is a signature of defects in the graphitic lattice [34]. The D band activates near the edge or the defects and attributed to a double resonance Raman scattering process [35,36]. Increasing the density of defects in the honeycomb sp^2 lattice gives rise to another well-known forbidden double resonance, the D′ band (at ~1610 cm ^{1}) [37,38]. That is why monitoring the relative changes in the D and D′ bands with respect to the G band in Raman spectra allows deductions about the presence and evolution of defects within the graphitic lattice. The D′ is the intra-valley scattering process, whereas D band is associated with the inter-valley scattering version [38,39]. Thus monitoring D band and D′ band gives tremendous information on the defect generation on the graphitic lattice.

Defects in graphitic materials have been modeled in two ways: zero-dimensional point like defect (sp^3-hybridization, vacancy like defect/hetero-atom doping, ion-bombardment etc.) and one-dimensional line-defects (heat treatment, mechanical strain etc.). Generally, line defects in a graphitic structure can be separated in two different categories: grain boundaries and dislocations type [40,41]. Tilted boundaries separating two domains of different lattice orientations with the tilt axis normal to the plane are known as grain boundaries. Orientational mismatch between two domain connected through a non-straight GGB, consists of 5–7 pentagon-heptagon pairs are common boundary structure of a graphitic lattice [42]. On the other hand, a couple of 5–7 pairs oriented at 90° and connected by dangling bonds or missing carbon chain constitutes dislocation defects [41,43]. Both above mentioned line defects contribute to crystallite size in a graphitic lattice. Pictorial representation of the model is represented in Fig. 1, where L_D represents the average distance between point defects whereas L_a represents average crystallite size or related to the average crystallite area (L_a^2). In this scenario, a perfect graphitic structure is defined as $L_D \to \infty$, $L_a \to \infty$, while a fully disordered graphitic structure as represented by $L_D \to 0$, $L_a \to 0$ [44,45]. All the graphitic structures which are imperfect, *e.g.* multiwalled carbon nanotube, graphene nano-flakes, graphene oxides, doped graphene etc. fall under the above-mentioned limit. The density of point and/or line-defects can be estimated from the ratio of the integrated area of the D band (A_D) to that of the G band (A_G). Together with the G band line-width (Γ_G), the ratio $(A_D/A_G)E_L^4$ (E_L- excitation laser energy) forms a Raman map which provides a much better understanding of the nature of the defects [44]. Additionally, the ratio between intensity of D band to that of D′ band ($I_D/I_{D'}$) allows to identify the type of point defects can are present in a graphitic lattice [39].

In this paper, first we briefly talk about our application of the point and line-defect model to graphitic honeycomb structures. We will discuss the combined effects of defect distributions on the Raman map. As a proof of concept, we have taken a widely used graphitic nanostructure, multiwalled carbon nanotubes (MWCNT) as our starting material and experimentally measured the values of $(A_D/A_G)E_L^4$ and $I_D/I_{D'}$. We have proceeded our investigation by further functionalizing MWCNTs through refluxing them in a mixture of concentrated nitric acid and concentrated sulfuric acid. This treatment results in the generation and growth of both point- and line-like defects in the graphitic lattice. This leads to an ever-growing number of functional groups – i.e., defects – being introduced over time. This allowed us to prepare samples with increasing defect density by increasing the reaction time.

Controlling the duration of the functionalization reaction, we have monitored the number of defects embedded in the graphitic structure. By plotting the Raman phase areas together with $I_D/I_{D'}$ -graphs at different stages of functionalization, we have experimentally corroborated our postulate. Functionalized MWCNTs (f-MWCNT) were then used as a matrix to incorporate transition metal nanoparticles (TMNs). We have prepared the catalytic cathodes from this modified f-MWCNT-TMNs, and used them in ORR electrochemistry [46]. Catalytic redox reactions have been carried out under two different electrochemical environments, using potassium hydroxide (KOH) and sodium chloride (NaCl) as electrolytes. We derived the type of defects present in the f-MWCNT matrix over a large number of electrochemical cycles by monitoring the Raman phase area. The exact defect evolution pathways on the graphitic structure after prolonged electrochemical cycling have been analyzed in light of the Raman phase map and $I_D/I_{D'}$.

2. The Raman phase map and Raman ellipse

Point and line defects are two typical sets of defects in a graphitic

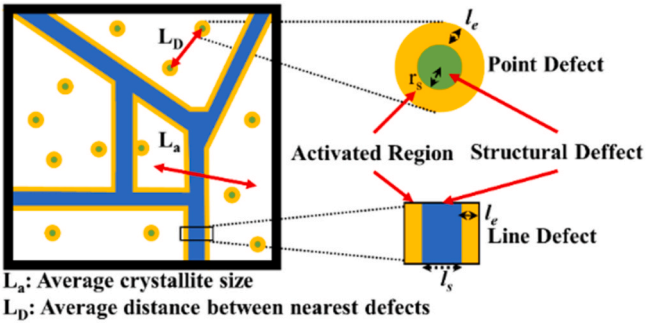

Fig. 1. Illustration of a graphitic lattice containing point-like and line defects present in a defective honeycomb arrangement. (A colour version of this figure can be viewed online.)

framework. Point defects are characterized by the average distance between two nearest point-like defects (L_D) or by the defect density ($\sim 1/L_D^2$) (Fig. 1). Line defects are specified by their average crystallite size (L_a) or by crystallite area (L_a^2). Disorder introduced by defects causes broadening, shifting, and increases the asymmetry of the Raman bands. The G band is arising from the graphitic structure, so the line-width of the G band (Γ_G) increases with increasing defect density and decreases with growing average crystallite size [44,47,48]. This phenomenon can be represented as

$$\Gamma_G(L_a, L_D) = \Gamma_G(\infty) + 87\exp(\quad \xi / l_{ph}) \tag{1}$$

where ξ represents phonon localization length, l_{ph} represents phonon coherence length (~16 nm), $\Gamma_G(\infty)$ is line-width of G band without any defect (~15 cm ^{1}) [44]. The phonon localization length is found to be $\xi = L_a$ for samples with pure line defect or $\xi = 10L_D$ for samples with pure point defect. When both are present, ξ is set to the larger value of either L_a or $10L_D$.

The local environment of the defective-region has a greater effect on the area under the G band and D band. So careful characterization of the defect is required. In Fig. 1, r_s depicts the radius of the defect (green area) whereas l_e is electron coherence length surrounding r_s where the region is activated due to the presence of defect. The line defect is characterized by l_s (Fig. 1 blue region), and is surrounded by l_e region where the effect of line defect is prominent. In case only point-like defects are present, the $(A_D/A_G)E_L^4$ is given by the relation below [44],

$$\left(\frac{A_D}{A_G}\right)E_L^4(L_D) = C_S^{0D}\left(1 \quad e^{-\frac{\pi r_s^2}{L_D^2}}\right) + \frac{2\pi}{L_D^2}C_A^{0D}l_e(l_e + r_s)e^{-\frac{\pi r_s^2}{L_D^2}} \tag{2}$$

The terms C_S^{0D} and C_A^{0D} are the coefficients simultaneously contributing from the damaged region and the activated region in the absence of line defects.

For line-like defects, $(A_D/A_G)E_L^4$ is represented as

$$\left(\frac{A_D}{A_G}\right)E_L^4(L_a) = \frac{1}{L_a^2}\left[4C_S^{1D}l_S(L_a \quad l_S) + 2C_A^{1D}l_e(L_a \quad 2l_s) \times \left(1 \quad e^{-\frac{L_a \quad 2l_s}{l_e}}\right)\right] \tag{3}$$

Similarly, C_S^{1D} and C_A^{1D} are coefficients contributing from the damaged region and the activated region, respectively, in the absence of point defects. When both point-like defects and line-defects are present in the graphitic lattice the ratio $(A_D/A_G)E_L^4$ can be represented as,

$$\left(\frac{A_D}{A_G}\right)E_L^4(L_a, L_D) = C_S^{0D}\left(1 \quad e^{-\frac{\pi r_s^2}{L_D^2}}\right) + \frac{2\pi}{L_D^2}C_A^{0D}l_e\frac{(l_e + r_s)}{L_D^2}\left[1 \right.$$
$$\left. 4l_s\frac{L_a \quad l_s}{L_a^2}\right]e^{-\frac{\pi r_s^2}{L_D^2}} + 4C_S^{1D}l_S\frac{(L_a \quad l_S)}{L_a^2}e^{-\frac{\pi r_s^2}{L_D^2}} + 2C_A^{1D}l_e(L_a \quad 2l_s) \times \left(1 \right.$$
$$\left. e^{-\frac{L_a \quad 2l_s}{l_e}}\right)e^{-\frac{\pi r_s^2}{L_D^2}} \tag{4}$$

the values of all the parameters to calculate Raman map are listed in Table SI [44].

Fig. 2(a) depicts a generic Raman map, where four distinct combinations of L_a and L_D are represented as dots inside the Raman map, with

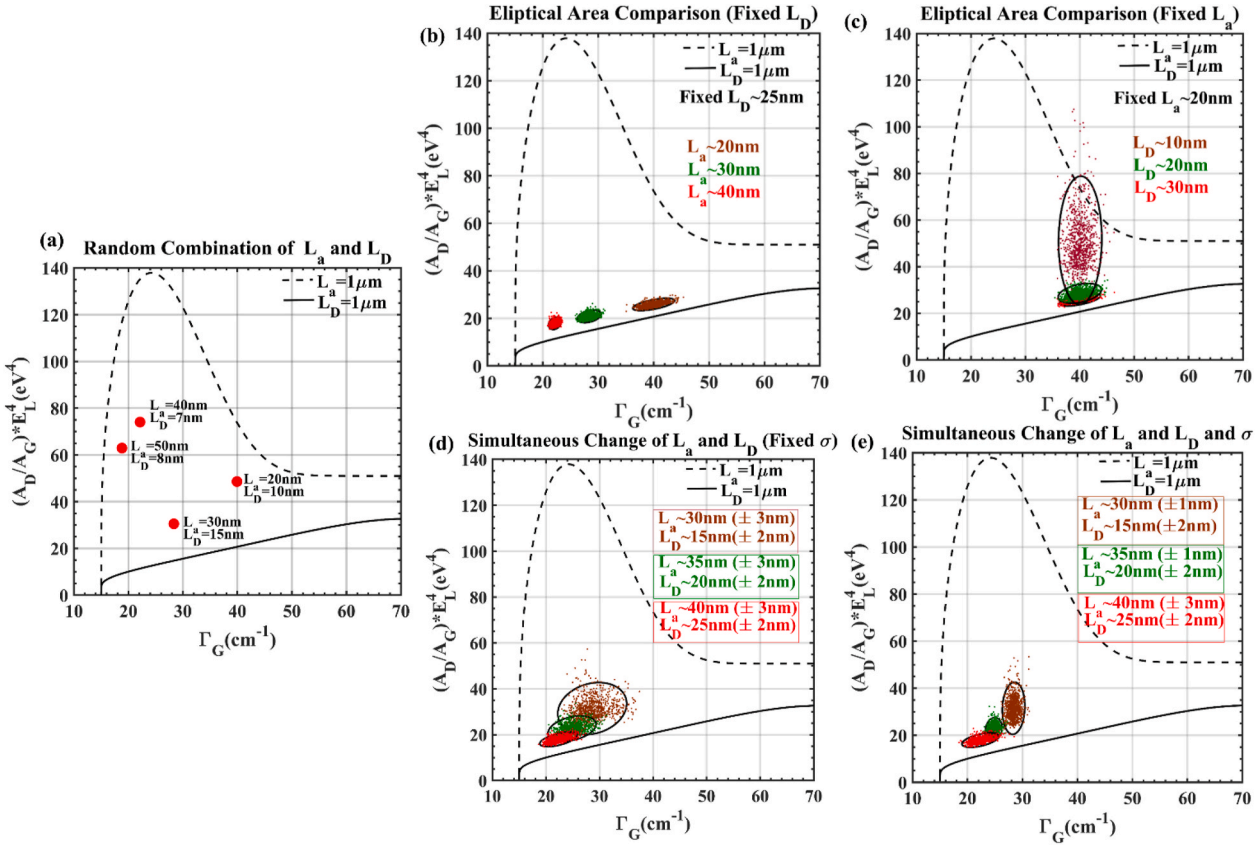

Fig. 2. Theoretical Raman phase maps of $(A_D/A_G)E_L^4$ as a function of G band line-width for two extreme cases L_a and L_D as 1 μm are presented. (a) A depiction of different combinations of L_a and L_D is showing the distributive pattern created on the Raman phase map. Each individual dot represents given sets of L_D and L_a. (b) Fixed L_D with varying L_a, the Raman ellipses orient horizontally for only line defects. (c) Fixed L_a with varying L_D, in contrary to previous, the Raman ellipses orient vertically for only defect in point-like case. (d) Both L_a and L_D have been parameterized, keeping the defect distribution fixed. Here σ, in first bracket, presents the value of the standard deviation which has been applied to generate the data points which follows a normal distribution (e) All the parameters L_a, L_D and their distributions (values of σ) have been varied which resembles real physical situation.

the extreme crystallite values for L_a and L_D as 1 μm. In the mentioned Raman map, calculated values of $\left(\frac{A_D}{A_G}\right)E_L^4(L_a, L_D)$ are discussed in the light of a crystalline graphitic structure which has an average L_a and L_D.

However, a real-life sample will be composed of a host of MWCNTs of different lengths and composition, or of graphite-flakes of different sizes. Hence, L_a s and L_D s will constitute distributions of values rather than discrete data points. To account for this, we have taken a normal distribution of 900 crystallites, where L_a is the average of the distribution and the standard deviation (σ) of the distribution is kept constant at ±1 nm. Applied to the generation of the Raman map (Fig. 2(b)), this distribution results in clusters of data points centered around the mean value. Fig. 2(b), depicts a case where the average density of point defects is kept constant ($L_D = 25$ nm), while average density of line-defects (L_a) is varied around mean values of 40, 30 and 20 nm (signifying an increase in line-defect density). In Fig. 2(b) the calculated values of $\left(\frac{A_D}{A_G}\right)E_L^4(L_a, L_D)$ yield a densely packed distribution of points on Raman map, depending on their respective average L_a values. Notably, the trend of rising line-width (Γ_G) with increasing defect density (decrease in L_a) is also correctly reflected in the Raman map. The distribution of the individual data points of $\left(\frac{A_D}{A_G}\right)E_L^4(L_a, L_D)$ in the Raman map forms an elliptical shape. To better visualize the individual signal groups, ellipses have been drawn that enclose 95 % of the data points in each group. The area of the ellipse gives a correlation with the types of defects and their distribution in the graphitic structures. The distribution of defect densities is proportional to this elliptical area which is embedded in Raman phase area. In Fig. 2(c), the Raman map is generated by varying the average defect-separation (L_D) between 30, 20 and 10 nm (increasing point defect-density) while the crystallite defect length (L_a) is fixed at 20 nm. It is clear from the Raman map, that Γ_G does not change significantly as the point-defects contribute much less to it. On the other hand, the Raman phase areas and the ellipses constructed from $\left(\frac{A_D}{A_G}\right)E_L^4(L_a, L_D)$ are quite informative on the amount of defect and its distribution. Comparing both Fig. 2(b) and (c), we see a stark distinction in the Raman phase areas between selectively varying the distribution of line-defects and point-defects, respectively. In the 'line-defect' case, the Raman area ellipses lie horizontally in the phase plot, whereas they are spread vertically when point-like defects are predominant.

In subsequent simulations (Fig. 2(d and e)), we varied both L_a and L_D with the spread distribution set to between ±1 and ± 3 nm. From Fig. 2 (d), keeping the distribution range constant, we can derive that the Raman phase area grows bigger as the average L_D decreases. In Fig. 2(e) three separate cases are presented, where each case the distribution range has been varied from the previous instances. This situation can be modeled closely to a real situation, as not only the average defect length varies from sample to sample but also the defect range. In phase map Fig. 2(e), the orientations of the Raman area ellipses are all different from Fig. 2(d) which relays the information on the state and distribution of the defects. The larger σ of the point defects (L_D) generates Raman ellipses which are oriented vertically, and horizontally oriented Raman ellipses are created with a larger σ of the line defects (L_a). We can conclude from these Raman maps and Raman phase areas representations, that the changes in Γ_G are largely dependent on the average line defects, whereas the areas and orientations of the Raman phase ellipses are highly sensitive to the point defect in the graphitic nanostructures.

3. Sample preparation

The MWCNT was bought from Sigma Aldrich and used for further treatment without any purification. The detailed characterization of the MWCNT is discussed in the supporting information section "Characterization of MWCNT". To prepare MWCNTs with varying defect distributions, the commercially obtained material was further functionalized as follows. In a typical synthesis, 250 mg of MWCNT were placed in a 100 mL flask. 25 mL ice cooled concentrated sulfuric acid were added and the reaction mixture was stirred by magnetic stirrer. Slowly, 10 mL of fuming nitric acid (concentrated) were added via the reflux condenser. The reaction mixture was heated to 85 °C and refluxed for 10, 30 and 120 min. The reaction mixture was filtered off with glass frit and the f-MWCNTs were washed with demineralized water until the filtrate showed a neutral pH. The collected f-MWCNTs were then dried for 24 h at 80 °C. Fig. S4 shows the results of IR-measurements conducted with a FTIR-ATR from PerkinElmer Spectrum 2 with a spectral resolution of 0.5 cm^{-1}. The spectra show the typically signals of functional groups on the MWCNT-Surface from the functionalization with acids.

The PtNiCoFe catalyst on *f*-MWCNT was synthesized as described in our previous work [46]. In brief, *f*-MWCNT (100 mg) were dispersed in 200 mL ethylene glycol and water (1:1) mixture, by stirring for 12 h at room temperature. 3.8 ml each of 0.05 M solutions of H_2PtCl_6, $Fe(NO_3)_2$, $Ni(NO_3)_2$ and $Co(NO_3)_2$ were then added and the mixture was stirred for another 24 h. The pH of the resulting suspension was adjusted to 11 via addition of 2.5 M aqueous NaOH and the mixture was heated to 50 °C. 50 mL of a 0.1 M $NaBH_4$-solution was added dropwise over 1 h. After complete addition, the solution was stirred for another 12 h and the resulting black precipitate was collected by filtration and washed with demineralized water. The isolated black powder was sintered at 300 °C in a vacuum oven for 2 h.

The electrochemical measurements were performed at room temperature in a three-electrode setup using a bipotentiostat WaveDriver20 together with a rotating ring-disc electrode-setup (RRDE) from Pine Research Instruments. Pt-wire was used as counter electrode and 3.5 M Ag/AgCl served as reference electrode. A glassy carbon working electrode with a surface area of 0.19635 cm^2 was used, which was coated with 5 μL of catalyst ink. The ink was prepared by adding 20 mg of the active material (MWCNT, f-MWCNT, PtFeNiCo@ f-MWCNT) to a mixture of 50 μL Nafion suspension and 1950 μL ethanol. The ink was stirred for 24 h and treated in an ultrasonic bath for 10 min before use.

Cyclic voltammetry analyses of the functionalized MWCNTs were performed in N_2 rinsed 0.1 M KOH solution over a potential range of 350 to 950 mV vs. Ag/AgCl at a scan speed of 50 mV s^{-1}. Cyclic voltammetry of the metal catalyst was conducted in N_2 rinsed 0.1 M KOH and 0.1 M NaCl solution after 100, 200, 300, 500 and 1000 ORR-cycles (O_2 rinsed electrolytes) within the same voltage window.

Fig. S5 shows the results from cyclic voltammetry in 0.1 M KOH of f-MWCNTs functionalized with different reaction times. As expected, with the increase in the structural defect-density, the capacitive behavior of the f-MWCNTs also increased. Figs. S6 and S7 show the electrochemical behavior of PtFeNiCo@ f-MWCNT in 0.1 M KOH and 0.1 M NaCl. Here the catalysts demonstrate a good stability in KOH and an even better stability in NaCl. However, the focus in this work stays on the Raman results and therefore we will not go into further electrochemical details.

4. Results and discussion

The acidic oxidation (see sample preparation in SI section) is a complex sequential process where MWCNTs are gradually oxidized which leads to the introduction of carboxyl, carbonyl or hydroxyl groups [49,50]. These oxygen-containing groups are mainly carboxyl, carbonyl or hydroxyl groups which break down the graphitic structure in MWCNTs by incorporating sp^3 carbon point defects. Prolonged oxidation causes MWCNTs to tear as it congregates the sp^3 defects with functionalization.

Fig. 3(a) reports Raman spectra from HOPG and electrode surface made from f-MWCNT at different functionalization stages. The Raman spectrum of HOPG shows a single G band (1580 cm^{-1}) and the material does not contain any defects as D and D′ bands are absent. Conversely, MWCNT and f-MWCNTs show broader G bands and noticeable D and D′ bands. The D band peaks are located near 1335 cm^{-1} whereas the D′ peaks are observed at 1615 cm^{-1}. At a glance, the relative intensity of

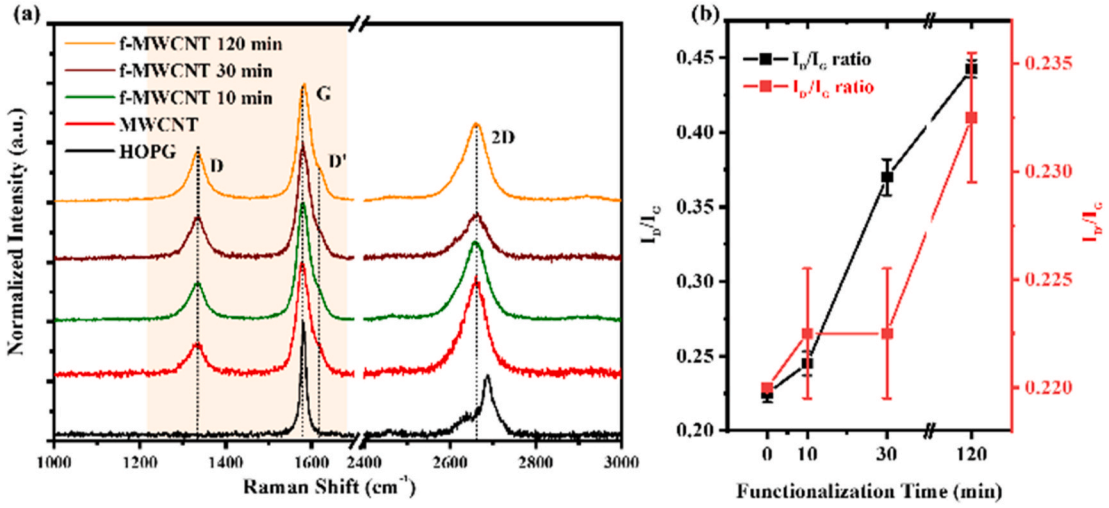

Fig. 3. (a) Raman spectrum of HOPG and defective f-MWCNT showing their respective D, G, D′ and 2D bands. (b) I_D/I_G and $I_{D'}/I_G$ of respective f-MWCNT advocating increase in the defect density and defect distributions.

the D band peak increases with the duration of oxidation. But to have a comprehensive viewpoint, we have to rely on the statistical Raman analysis (see Raman data collection and analysis in SI section). Series of collected spectra from the electrode surfaces have therefore been analyzed to get statistical distributions of the G, D and D′ band peak positions along with line-width of the G band (Γ_G) and the $I_D/\ I_G$ ratio.

Raman maps compiled in Fig. S8 of an electrode surface prepared by using 120 min f-MWCNT visualizes its intrinsic inhomogeneity. This feature of the surfaces was observed for all the electrodes. The histograms of the band's peak positions and the line-width s of the respective bands depicted in Fig. S9 closely resemble normal distributions, and are therefore suitable for statistical analysis by the model presented in Fig. 2. The conclusions from these statistical analyses are summarized in Fig. S10. Notably, the peak frequencies of all bands are blue-shifted and there is an increased broadening in the subsequent line-width of the Raman bands, as the density of defects in the graphitic surface increases. The broadening of the G band (from 32 cm^{-1} to 36 cm^{-1}) is easily noticeable (Fig. 3(b)), although the other bands remain practically unaltered. We explain this observation with the amorphization process of the graphitic lattice to nanocrystalline graphite, containing almost ~0 % sp^3 hybridized carbon [51]. The I_D/I_G ratio increases from 0.22 to 0.45. Despite this drastic increase compared to the pristine material, the value still remains far below the limit of the low defect concentration regime ($I_D/I_G < 3$) [51]. Even after the oxidation the material therefore retains coherent graphitic structures large enough that information from individual defects is not entirely lost. This would, however, be expected in the highly disordered regime ($I_D/I_G > 3$) where defects are abundant and too close to each other [52].

The Raman phase plots of pristine MWCNT and f-MWCNT (Fig. S11) show clear distribution patterns corresponding to the different functionalization times. These distributions create Raman area ellipses which are reminiscent of the simulated patterns shown in Fig. 2. Note that the distribution points lie outside the enclosed area created by $L_a = 1\ \mu m$ and $L_D = 1\ \mu m$. This is because these simulated boundary lines are created using parameters from pristine graphene. In Fig. S7 (b), note that the line-width of the G band (Γ_G) is increasing with increasing functionalization time. Fig. 4(a) is a close-up view which elucidates the processes involved in the functionalization time. The Raman ellipse before functionalization is horizontal in the Raman phase map, indicating that the distribution of line defects is the limiting factor in the starting material. After 10 min functionalization, the Raman area ellipse becomes tilted and after 30 min functionalization its orientation is completely vertical. In the last sample *i.e.* after 120 min of functionalization, the orientation of the ellipse again comes back to horizontal.

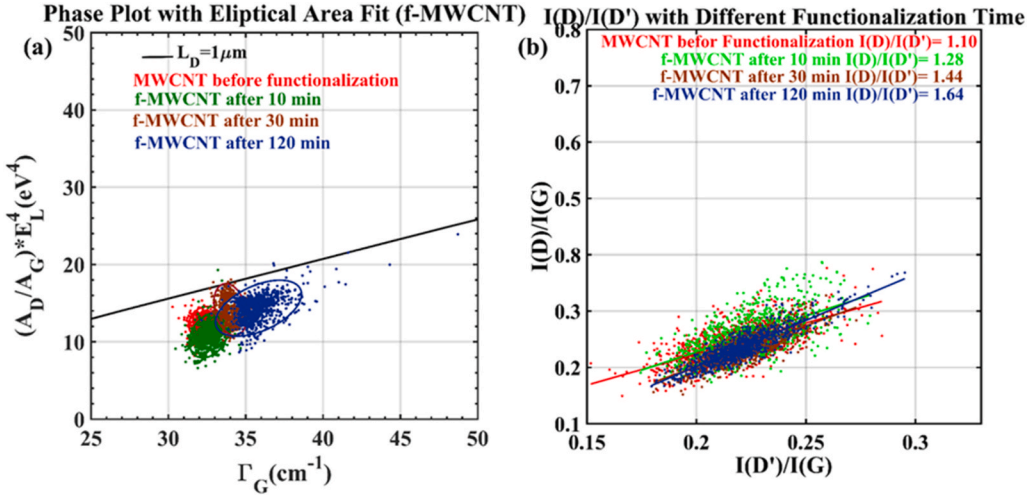

Fig. 4. (a) Amplified Raman phase plot of f-MWCNT showing the exact defect generation pathway through the orientation of the Raman ellipse. (b) Linear fit to calculate I_D/I_D from I_D/I_G relative to $I_{D'}/I_G$ plot in different stages of functionalization.

Though the I_D/I_G ratio provides a reasonable indication of the purity of the graphitic lattice, it does not contain information on the type of defect imbedded in the lattice [37,39]. In contrast, $I_D/I_{D'}$ indicates the nature of defects in a graphitic lattice because I_D more strongly correlates with the presence of sp^3-type defects than with vacancy-like and grain-boundary size defects. Fig. 4(b) depicts I_D/I_G with respect to $I_{D'}/I_G$, and the slope of the linear fit corresponds to the $I_D/I_{D'}$ ratio. For the pristine MWCNTs $I_D/I_{D'}$ is near 1.10, which resides well below the grain-boundary type defects (value ~3.5), confirming the graphitic lattice is nanocrystalline in nature [39,51]. Investigations on graphene containing mainly sp^3-type defects generated e.g. by fluorination show a high $I_D/I_{D'} \approx 13$ [39]. In our measurements, the value of $I_{D'}/I_D$ increases monotonically in successive oxidation stages and reaches to $I_{D'}/I_D$ ~1.64 after 120 min of oxidation. Previous work on the acid treatment of MWCNT reports ID/ID' value for 1 h is 1.2 and 3 h is 1.82 which are relatively close with our statistically obtained values [53]. The authors have attributed the defects generated on the wall of MWCNT as several types of 5–7 Haeckelite structure. This infers that the sp^3-type defect in oxidation of MWCNT is usually not isolated, but it appears in form of clusters or islands and behaves like a dislocation boundary type defect. B. W. Jeong et al. shows that dislocation defects with two 5–7 pairs consisting of dangling bond (sp^3-carbon) are energetically preferred to the local Haeckelite structure when the number of point vacancy defect increases to more than ten [43]. The dislocated chain is energetically further relaxed when the carbon atoms in between two 5–7 pair are missing carbon chain. The observation from the Raman phase map and $I_D/I_{D'}$ leads to the diagnosis that, in the beginning stages of functionalization, sp^3-like defects start to appear, whereas at the latter stages of the process, the sp^3-like defects merge to form dislocation boundary-like defects [43,54]. Keeping these findings in mind, we can assume, prolonged sp^3 formation through chemical reaction such as oxidation, fluorination, chlorination of graphitic structure leads to dislocation type topological defect (Fig. S12).

Further statistical Raman analyses were carried out on the electro cycled cathodes of f-MWCNT loaded with transition metal nanoparticles (f-MWCNT-TMN). Fig. S13 shows the statistical Raman analysis of f-MWCNT-TMN cycled in KOH medium, while the Raman phase plots of these electrodes are depicted in Fig. 5(a). The changes in the value of the I_D/I_G ratio over the course of cycling are marginal, suggesting very minor structural changes. Contrarily, the Raman phase map shows clear changes in the defect arrangement in successive electrochemical cycles. Initially, the Raman ellipse of the pristine electrode lies diagonally with a downward slope. As the electrochemical cycling proceeds, the ellipses adopt flatter orientations and the average line-line-width of the G band exhibits a slight decrease from the starting value. This can be attributed to the reduction of the density of boundary-like line-defects in the graphitic lattice. In addition, the $I_D/I_{D'}$ value also decreases from 1.63 to 1.05 (Fig. 6(a)) as the cycling of the electrode proceeds. This suggests an effective reduction of sp^3-like defects. Previous studies showed that self-healing occurs in ion bombarded graphene (containing mainly vacancy-like point-defects) under thermal annealing. This was attributed to the recombination of mobile carbon adatoms with vacancies near grain-boundaries [55,56]. Highly mobile adatoms, generated from ion bombardment, are presumed to be anisotropically transported to grain-boundaries due to higher enthalpy of the grain-edge compared to honeycomb lattice. Accumulation of carbon adatoms then prompts a preferential self-healing at the grain-boundaries and increases the effective crystallinity in the graphitic lattice as a whole [56]. In our case, during rigorous ORR cycling in a KOH electrolyte, the highly basic reaction conditions cause sp^3 carbons to be oxidized [1,57,58]. This generates excess carbon atoms on the graphitic lattice (adatoms) on the sp^3-like defect centers which then enable self-healing of defects [59–61]. These newly formed adatoms migrate to line-like defective regions and reconstructs the f-MWCNT which is evidenced by the changes of the Raman ellipse and $I_D/I_{D'}$.

A completely different scenario of defect evolution in nano-graphitic lattice is observed when the ORR cycling is performed in an NaCl electrolyte. The summarized results from statistical Raman analysis of the respective G, D and D' bands are presented in Fig. S14. The I_D/I_G and $I_{D'}/I_G$ values again remain almost unchanged throughout the ORR cycling steps. The average linewidth of the G band remains in the phase map (Fig. 5 (b)). This finding indicates that there is clear absence of self-healing of the nano-graphitic lattice under ORR conditions in NaCl, while self-healing was observed in the KOH electrolyte. Furthermore, the Raman ellipses in the phase plot (Fig. 5 (b)) convey the exact evolution of the defects in the electrocycling process. In the beginning, the orientations of the ellipses again show a downward slope, but end up with a near vertical orientation. This conjecture is corroborated by the corresponding $I_D/I_{D'}$ plot in Fig. 6 (b). During ORR cycling in NaCl medium the $I_D/I_{D'}$-slope shows a gradual increase from 1.61 to 1.87 from 0 to 500 cycles, but jumps to 4.45 after 1000 cycles. Though the value is markedly lower than that of pure sp^3-type- or vacancy-defects ($I_D/I_{D'} \approx 7$) in defective graphene [39,62], it suggests that after prolonged cycling in NaCl, there is incorporation of the point like defect in the

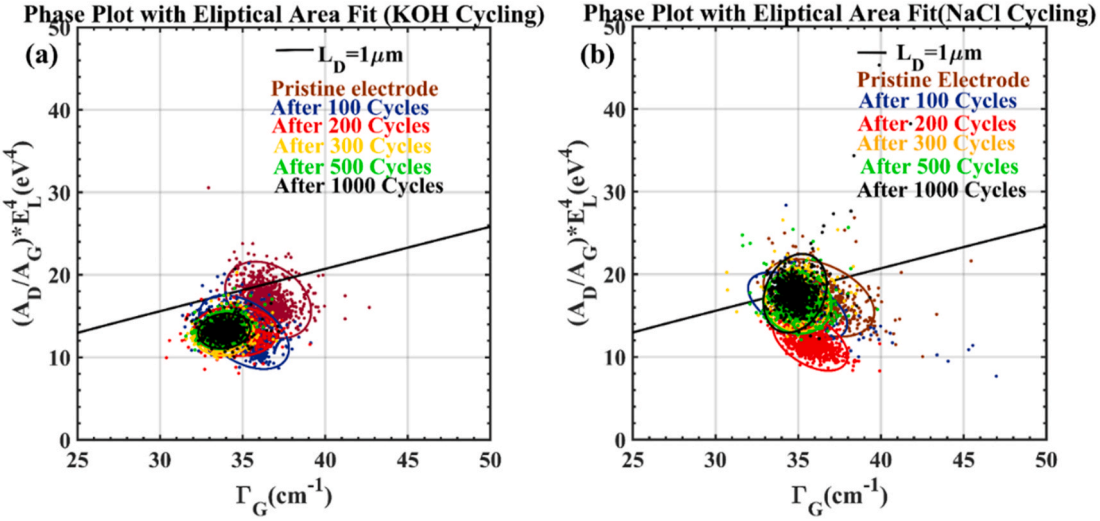

Fig. 5. Variation of the Raman ellipse resulting from two different electrochemical cycling processes have been presented. (a) ORR cycling of f-MWCNT matrix under KOH electrolyte, evidencing grain-boundary reformation by preferential self-healing and (b) ORR cycling under NaCl electrolyte, indicating sp^3-type defect generation. (A colour version of this figure can be viewed online.)

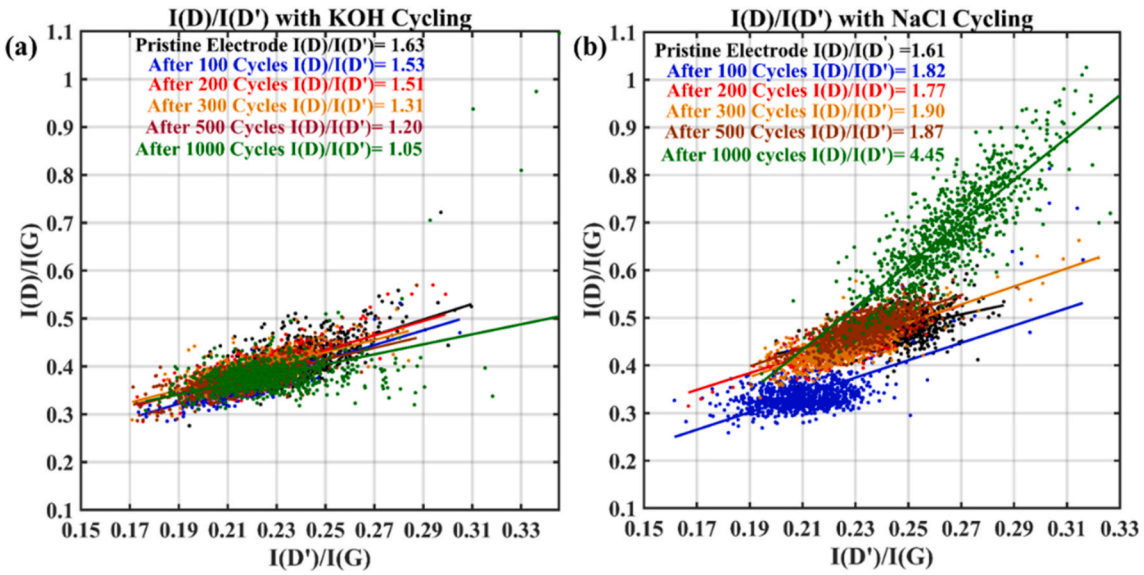

Fig. 6. Progress of I_D/I_D ratio of f-MWCNT nano-graphitic lattice after electrochemical cycling in (a) KOH and (b) NaCl shows the content of sp^3-type defect evolution.

nano-graphitic lattice of f-MWCNT. Previously, the electrochemical chlorination of graphene has been demonstrated using 1.5 M NaCl (aq.) for the *in situ* electrochemical generation of trace amounts of chlorine radicals at the graphene surface [62]. A similar process might be at play here. Hydroxyl radicals formed during ORR may oxidize chloride anions to chloride radicals, which then chlorinate the graphene. This would account for the detected increase in (sp^3-) point-defects.

5. Conclusion

In conclusion, the evolution of defects in MWCNTs during oxidative functionalization and electrochemical cycling has been investigated by statistical Raman spectroscopy and analysis of the corresponding Raman phase maps with the Raman ellipse model were performed. Defects in the pristine MWCNTs are predominantly line-like (grain boundaries) in character rather than point-like (sp^3-type, vacancy etc.) as the orientation of the Raman ellipse is horizontal (Fig. 4(a)).

Modification by rigorous oxidation of the carbon (10–30min functionalization, Fig. 4 (a)) induced the formation of sp^3-type point defects, as conclusively evidenced by the orientation of the Raman ellipse and I_D/I_D representations. At this instance, the defect density is still very low. At latter stages of oxidation, amalgamation of an increasing number of sp^3-type defects results in boundary-type defects. Furthermore, our subsequent study on the defect evolution of the f-MWCNTs under electrocatalytic ORR conditions, unveiled contrasting scenarios depending of the nature of the electrochemical environment. When the catalysis is performed in aqueous KOH as reaction condition, incremental increase of the average crystallite length (L_a) has been observed which might be linked to self-healing near crystallite grain-boundary (Fig. 7). In contrast, when the catalysis is carried out in NaCl solution, the orientation of the Raman ellipse together with changing slope in the I_D/I_D plot signifies an increase in sp^3-type defect generation – likely through electrochemical chlorination.

The Raman ellipse in combination with I_D/I_D is a new and powerful analytical tool to map defects in a graphitic lattice more precise than by mere plotting of only I_D/I_G. Notably, application of this analytical

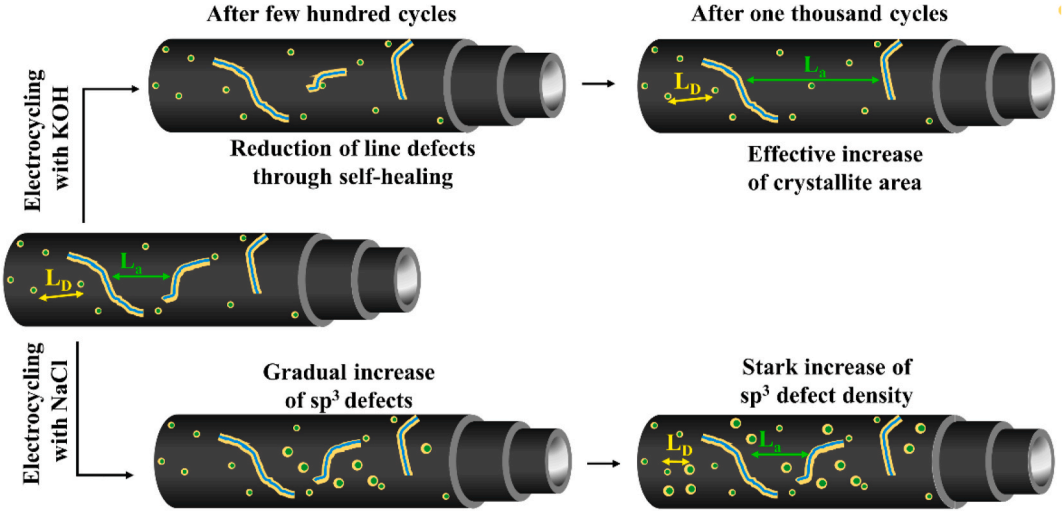

Fig. 7. Schematic representation of the nano-graphitic structural transformation of the f-MWCNT matrix during prolonged electrochemical cycling under two different ORR conditions. The average crystallite size increases in KOH medium whereas the sp^3-like defects are increasing in NaCl medium. (A colour version of this figure can be viewed online.)

technique can be particularly useful to derive the exact nature of the predominant defects and to monitor the defect evolution in materials during exposure to chemical, electrochemical or mechanical stress.

The Raman phase map created from graphene or graphene-based material and adapting it to MWCNT systems provides a reasonable overview of the evolution of the defect on MWCNT based system. To use the arguments on single wall carbon nanotube is still not ideal (see SI "Acid treatment of SWCNT"). The limitation comes from the complexity regarding the G-band due to phonon confinement along the SWCNT circumferential direction. In that regard, finding exact $I_D/ I_{D'}$ for acid oxidation is difficult. Not only that, further studies regarding ion bombardment, vacancy type, annealing are also required to establish this technique as unique technique for studying of defects on CNT. Further studies and careful evaluation of all the parameters are also required for CNTs.

CRediT authorship contribution statement

Sirshendu Dinda: Conceptualization, Methodology, Experiment, Data curation, Writing – original draft, preparation, Writing – review & editing. **Tobias Braun:** Experiment, Methodology, XPS analysis, Writing – original draft. **Frank D. Pammer:** Investigation, Writing – original draft, preparation and Reviewing. **Jaehoon Choi:** TEM image analysis. **Simon Fleischmann:** TEM image analysis, Writing- Reviewing. **Maximilian Fichtner:** Writing – review & editing.

Declaration of competing interest

The manuscript has been prepared with permission from all the authors. The authors declare no competing financial interest.

Acknowledgements

This work contributes to the research performed at CELEST (Center of Electrochemical Energy Storage Ulm-Karlsruhe) and was partially funded by German Research Foundation (DFG) under project ID 390874152 (POLiS Cluster of Excellence). J.C. and S.F. acknowledge funding from the German Federal Ministry of Education and Research (BMBF) in the "NanoMatFutur" program (grant No. 03XP0423) and financial support from the Helmholtz Association.

References

[1] M. Armand, J.M. Tarascon, Building better batteries, Nature 451 (2008) 652–657.
[2] D. Larcher, J.M. Tarascon, Towards greener and more sustainable batteries for electrical energy storage, Nat. Chem. 7 (2015) 19–29.
[3] Y.M. Chen, X.Y. Yu, Z. Li, U. Paik, X.W. Lou, Hierarchical MoS2 tubular structures internally wired by carbon nanotubes as a highly stable anode material for lithium-ion batteries, Sci. Adv. 2 e1600021..
[4] G. Huang, F. Zhang, X. Du, Y. Qin, D. Yin, L. Wang, Metal organic frameworks route to in situ insertion of multiwalled carbon nanotubes in Co3O4 polyhedra as anode materials for lithium-ion batteries, ACS Nano 9 (2015) 1592–1599.
[5] S.A. Freunberger, True performance metrics in beyond-intercalation batteries, Nat. Energy 2 (2017), 17091.
[6] J. Luo, J. Liu, Z. Zeng, C.F. Ng, L. Ma, H. Zhang, J. Lin, Z. Shen, H.J. Fan, Three-dimensional graphene foam supported Fe3O4 lithium battery anodes with long cycle life and high rate capability, Nano Lett. 13 (2013) 6136–6143.
[7] Z. Li, S. Wu, W. Lv, J.-J. Shao, F. Kang, Q.-H. Yang, Graphene emerges as a versatile template for materials preparation, Small 12 (2016) 2674–2688.
[8] L. Wang, J. Han, D. Kong, Y. Tao, Q.-H. Yang, Enhanced roles of carbon architectures in high-performance lithium-ion batteries, Nano-Micro Lett. 11 (2019) 5.
[9] W. Lv, Z. Li, Y. Deng, Q.-H. Yang, F. Kang, Graphene-based materials for electrochemical energy storage devices: opportunities and challenges, Energy Storage Mater. 2 (2016) 107–138.
[10] F. Xie, Z. Xu, Z. Guo, M.-M. Titirici, Hard carbons for sodium-ion batteries and beyond, Progress in Energy 2 (2020), 042002.
[11] Y. Jin, S. Sun, M. Ou, Y. Liu, C. Fan, X. Sun, J. Peng, Y. Li, Y. Qiu, P. Wei, Z. Deng, Y. Xu, J. Han, Y. Huang, High-performance hard carbon anode: tunable local structures and sodium storage mechanism, ACS Appl. Energy Mater. 1 (2018) 2295–2305.
[12] X. Chen, Y. Zheng, W. Liu, C. Zhang, S. Li, J. Li, High-performance sodium-ion batteries with a hard carbon anode: transition from the half-cell to full-cell perspective, Nanoscale 11 (2019) 22196–22205.
[13] C. Zhang, W. Lv, Y. Tao, Q.-H. Yang, Towards superior volumetric performance: design and preparation of novel carbon materials for energy storage, Energy Environ. Sci. 8 (2015) 1390–1403.
[14] M.-J. Lee, E. Lho, P. Bai, S. Chae, J. Li, J. Cho, Low-temperature carbon coating of nanosized Li1.015Al0.06Mn1.925O4 and high-density electrode for high-power Li-ion batteries, Nano Lett. 17 (2017) 3744–3751.
[15] H. Wei, Y. Liu, X. Zhai, F. Wang, X. Ren, F. Tao, T. Li, G. Wang, F. Ren, Application of carbon nanotube-based materials as interlayers in high-performance lithium-sulfur batteries: a review, Front. Energy Res. 8 (2020).
[16] J. Song, C. Wei, Z.-F. Huang, C. Liu, L. Zeng, X. Wang, Z.J. Xu, A review on fundamentals for designing oxygen evolution electrocatalysts, Chem. Soc. Rev. 49 (2020) 2196–2214.
[17] N.-T. Suen, S.-F. Hung, Q. Quan, N. Zhang, Y.-J. Xu, H.M. Chen, Electrocatalysis for the oxygen evolution reaction: recent development and future perspectives, Chem. Soc. Rev. 46 (2017) 337–365.
[18] R. Devivaraprasad, N. Nalajala, B. Bera, M. Neergat, Electrocatalysis of oxygen reduction reaction on shape-controlled Pt and Pd nanoparticles—importance of surface cleanliness and reconstruction, Front. Chem. 7 (2019).
[19] A. Vazhayil, L. Vazhayal, J. Thomas, S. Ashok C, N. Thomas, A comprehensive review on the recent developments in transition metal-based electrocatalysts for oxygen evolution reaction, Appl. Surf. Sci. Advan. 6 (2021), 100184.
[20] C.C.L. McCrory, S. Jung, I.M. Ferrer, S.M. Chatman, J.C. Peters, T.F. Jaramillo, Benchmarking hydrogen evolving reaction and oxygen evolving reaction electrocatalysts for solar water splitting devices, J. Am. Chem. Soc. 137 (2015) 4347–4357.
[21] R. Ma, G. Lin, Y. Zhou, Q. Liu, T. Zhang, G. Shan, M. Yang, J. Wang, A review of oxygen reduction mechanisms for metal-free carbon-based electrocatalysts, npj Comput. Mater. 5 (2019) 78.
[22] L. Qu, Y. Liu, J.-B. Baek, L. Dai, Nitrogen-doped graphene as efficient metal-free electrocatalyst for oxygen reduction in fuel cells, ACS Nano 4 (2010) 1321–1326.
[23] Z.-H. Sheng, L. Shao, J.-J. Chen, W.-J. Bao, F.-B. Wang, X.-H. Xia, Catalyst-free synthesis of nitrogen-doped graphene via thermal annealing graphite oxide with melamine and its excellent electrocatalysis, ACS Nano 5 (2011) 4350–4358.
[24] Z.-H. Sheng, H.-L. Gao, W.-J. Bao, F.-B. Wang, X.-H. Xia, Synthesis of boron doped graphene for oxygen reduction reaction in fuel cells, J. Mater. Chem. 22 (2012) 390–395.
[25] J. Wang, R. Ma, Z. Zhou, G. Liu, Q. Liu, Magnesiothermic synthesis of sulfur-doped graphene as an efficient metal-free electrocatalyst for oxygen reduction, Sci. Rep. 5 (2015) 9304.
[26] X. Lu, W.-L. Yim, B.H.R. Suryanto, C. Zhao, Electrocatalytic oxygen evolution at surface-oxidized multiwall carbon nanotubes, J. Am. Chem. Soc. 137 (2015) 2901–2907.
[27] X. Wang, A. Dong, L. Chai, J. Ding, L. Zhong, T.-T. Li, Y. Hu, J. Qian, S. Huang, Abundant nanotube coated ordered macroporous carbon matrix with enhanced electrocatalytic activity, J. Power Sources 467 (2020), 228302.
[28] P. Stelmachowski, J. Duch, D. Sebastián, M.J. Lázaro, A. Kotarba, Carbon-based composites as electrocatalysts for oxygen evolution reaction in alkaline media, Materials (2021).
[29] R. Fang, K. Chen, L. Yin, Z. Sun, F. Li, H.-M. Cheng, The regulating role of carbon nanotubes and graphene in lithium-ion and lithium–sulfur batteries, Adv. Mater. 31 (2019), 1800863.
[30] Y. Zhao, L.P. Wang, M.T. Sougrati, Z. Feng, Y. Leconte, A. Fisher, M. Srinivasan, Z. Xu, A review on design strategies for carbon based metal oxides and sulfides nanocomposites for high performance Li and Na ion battery anodes, Adv. Energy Mater. 7 (2017), 1601424.
[31] J.A. Quezada Renteria, C. Ruiz-Garcia, T. Sauvage, L.F. Chazaro-Ruiz, J.R. Rangel-Mendez, C.O. Ania, Photochemical and electrochemical reduction of graphene oxide thin films: tuning the nature of surface defects, Phys. Chem. Chem. Phys. 22 (2020) 20732–20743.
[32] F. Yuan, C. Shi, Q. Li, J. Wang, D. Zhang, Q. Wang, H. Wang, Z. Li, W. Wang, B. Wang, Unraveling the effect of intrinsic carbon defects on potassium storage performance, Adv. Funct. Mater. 32 (2022), 2208966.
[33] M.S. Dresselhaus, A. Jorio, A.G. Souza Filho, R. Saito, Defect characterization in graphene and carbon nanotubes using Raman spectroscopy, Phil. Trans. Math. Phys. Eng. Sci. 368 (2010) 5355–5377.
[34] F. Tuinstra, J.L. Koenig, Raman spectrum of graphite, J. Chem. Phys. 53 (2003) 1126–1130.
[35] J. Maultzsch, S. Reich, C. Thomsen, Chirality-selective Raman scattering of the D mode in carbon nanotubes, Phys. Rev. B 64 (2001), 121407.
[36] R. Saito, A. Jorio, A.G. Souza Filho, G. Dresselhaus, M.S. Dresselhaus, M. A. Pimenta, Probing phonon dispersion relations of graphite by double resonance Raman scattering, Phys. Rev. Lett. 88 (2001), 027401.
[37] J.-B. Wu, M.-L. Lin, X. Cong, H.-N. Liu, P.-H. Tan, Raman spectroscopy of graphene-based materials and its applications in related devices, Chem. Soc. Rev. 47 (2018) 1822–1873.

[38] S. Lee, J.-W. Peng, C.-H. Liu, Probing plasma-induced defect formation and oxidation in carbon nanotubes by Raman dispersion spectroscopy, Carbon 47 (2009) 3488–3497.
[39] A. Eckmann, A. Felten, A. Mishchenko, L. Britnell, R. Krupke, K.S. Novoselov, C. Casiraghi, Probing the nature of defects in graphene by Raman spectroscopy, Nano Lett. 12 (2012) 3925–3930.
[40] O.V. Yazyev, S.G. Louie, Topological defects in graphene: dislocations and grain boundaries, Phys. Rev. B 81 (2010), 195420.
[41] F. Banhart, J. Kotakoski, A.V. Krasheninnikov, Structural defects in graphene, ACS Nano 5 (2011) 26–41.
[42] P.Y. Huang, C.S. Ruiz-Vargas, A.M. van der Zande, W.S. Whitney, M.P. Levendorf, J.W. Kevek, S. Garg, J.S. Alden, C.J. Hustedt, Y. Zhu, J. Park, P.L. McEuen, D. A. Muller, Grains and grain boundaries in single-layer graphene atomic patchwork quilts, Nature 469 (2011) 389–392.
[43] B.W. Jeong, J. Ihm, G.-D. Lee, Stability of dislocation defect with two pentagon-heptagon pairs in graphene, Phys. Rev. B 78 (2008), 165403.
[44] L. Gustavo Cançado, M. Gomes da Silva, E.H. Martins Ferreira, F. Hof, K. Kampioti, K. Huang, A. Pénicaud, C. Alberto Achete, R.B. Capaz, A. Jorio, Disentangling contributions of point and line defects in the Raman spectra of graphene-related materials, 2D Mater. 4 (2017), 025039.
[45] M.M. Lucchese, F. Stavale, E.H.M. Ferreira, C. Vilani, M.V.O. Moutinho, R. B. Capaz, C.A. Achete, A. Jorio, Quantifying ion-induced defects and Raman relaxation length in graphene, Carbon 48 (2010) 1592–1597.
[46] T. Braun, S. Dinda, G. Karkera, G. Melinte, T. Diemant, C. Kübel, M. Fichtner, F. Pammer, Multi-component PtFeCoNi core-shell nanoparticles on MWCNTs as promising bifunctional catalyst for oxygen reduction and oxygen evolution reactions, ChemistrySelect 8 (2023), e202300396.
[47] A. Merlen, J.G. Buijnsters, C. Pardanaud, A guide to and review of the use of multiwavelength Raman spectroscopy for characterizing defective aromatic carbon solids: from graphene to amorphous carbons, Coatings (2017).
[48] L.G. Cançado, A. Jorio, E.H.M. Ferreira, F. Stavale, C.A. Achete, R.B. Capaz, M.V. O. Moutinho, A. Lombardo, T.S. Kulmala, A.C. Ferrari, Quantifying defects in graphene via Raman spectroscopy at different excitation energies, Nano Lett. 11 (2011) 3190–3196.
[49] H. Yu, Y. Jin, F. Peng, H. Wang, J. Yang, Kinetically controlled side-wall functionalization of carbon nanotubes by nitric acid oxidation, J. Phys. Chem. C 112 (2008) 6758–6763.
[50] N.T. Hung, N.M. Tuong, E.G. Rakov, Acid functionalization of carbon nanofibers, Inorg. Mater. 46 (2010) 1077–1083.
[51] A.C. Ferrari, J. Robertson, Interpretation of Raman spectra of disordered and amorphous carbon, Phys. Rev. B 61 (2000) 14095–14107.
[52] E.H. Martins Ferreira, M.V.O. Moutinho, F. Stavale, M.M. Lucchese, R.B. Capaz, C. A. Achete, A. Jorio, Evolution of the Raman spectra from single-, few-, and many-layer graphene with increasing disorder, Phys. Rev. B 82 (2010), 125429.
[53] S.A. Curran, J.A. Talla, D. Zhang, D.L. Carroll, Defect-induced vibrational response of multi-walled carbon nanotubes using resonance Raman spectroscopy, J. Mater. Res. 20 (2005) 3368–3373.
[54] S. Osswald, M. Havel, Y. Gogotsi, Monitoring oxidation of multiwalled carbon nanotubes by Raman spectroscopy, J. Raman Spectrosc. 38 (2007) 728–736.
[55] J. Chen, T. Shi, T. Cai, T. Xu, L. Sun, X. Wu, D. Yu, Self healing of defected graphene, Appl. Phys. Lett. 102 (2013), 103107.
[56] P. Vinchon, X. Glad, G. Robert Bigras, R. Martel, L. Stafford, Preferential self-healing at grain boundaries in plasma-treated graphene, Nat. Mater. 20 (2021) 49–54.
[57] E. Raymundo-Piñero, P. Azaïs, T. Cacciaguerra, D. Cazorla-Amorós, A. Linares-Solano, F. Béguin, KOH and NaOH activation mechanisms of multiwalled carbon nanotubes with different structural organisation, Carbon 43 (2005) 786–795.
[58] J. Sun, H. Li, L. Feng, Y. Jia, Q. Song, K. Li, A novel treatment of carbon fibers with improving tensile strength to synthesize evenly distributed carbon nanotubes on their surface, Appl. Surf. Sci. 403 (2017) 95–102.
[59] K. VijayaSekhar, S.G. Acharyya, S. Debroy, V.P.K. Miriyala, A. Acharyya, Self-heal. Phenomena Graphene: Potent. Appl. 14 (2016) 364–370.
[60] L. Tsetseris, S.T. Pantelides, Adatom complexes and self-healing mechanisms on graphene and single-wall carbon nanotubes, Carbon 47 (2009) 901–908.
[61] A. Postl, P.P.P. Hilgert, A. Markevich, J. Madsen, K. Mustonen, J. Kotakoski, T. Susi, Indirect measurement of the carbon adatom migration barrier on graphene, Carbon 196 (2022) 596–601.
[62] W. Li, Y. Li, K. Xu, Facile, electrochemical chlorination of graphene from an aqueous NaCl solution, Nano Lett. 21 (2021) 1150–1155.